



HAL
open science

Spatiotemporal analysis for detection of pre-symptomatic shape changes in neurodegenerative diseases: Initial application to the GENFI cohort

Claire Cury, Stanley Durrleman, David Cash, Marco Lorenzi, Jennifer M Nicholas, Martina Bocchetta, John C. van Swieten, Barbara Borroni, Daniela Galimberti, Mario Masellis, et al.

► To cite this version:

Claire Cury, Stanley Durrleman, David Cash, Marco Lorenzi, Jennifer M Nicholas, et al.. Spatiotemporal analysis for detection of pre-symptomatic shape changes in neurodegenerative diseases: Initial application to the GENFI cohort. *NeuroImage*, 2019, 188, pp.282-290. 10.1016/j.neuroimage.2018.11.063 . inserm-01958916

HAL Id: inserm-01958916

<https://inserm.hal.science/inserm-01958916v1>

Submitted on 16 Jan 2019

HAL is a multi-disciplinary open access archive for the deposit and dissemination of scientific research documents, whether they are published or not. The documents may come from teaching and research institutions in France or abroad, or from public or private research centers.

L'archive ouverte pluridisciplinaire **HAL**, est destinée au dépôt et à la diffusion de documents scientifiques de niveau recherche, publiés ou non, émanant des établissements d'enseignement et de recherche français ou étrangers, des laboratoires publics ou privés.

Spatiotemporal analysis for detection of pre-symptomatic shape changes in neurodegenerative diseases: initial application to the GENFI cohort

Claire Cury^{a,b}, Stanley Durrleman^d, David M. Cash^{a,b}, Marco Lorenzi^{a,e}, Jennifer M Nicholas^{b,f}, Martina Bocchetta^b, John C. van Swieten^g, Barbara Borroni^h, Daniela Galimbertiⁱ, Mario Masellis^j, Maria Carmela Tartaglia^k, James B Rowe^l, Caroline Graff^{m,n}, Fabrizio Tagliavini^o, Giovanni B. Frisoni^p, Robert Laforce Jr^q, Elizabeth Finger^r, Alexandre de Mendonça^s, Sandro Sorbi^{t,u}, Sebastien Ourselin^{a,b,c}, Jonathan D. Rohrer^b, Marc Modat^{a,b,c}, on behalf of the Genetic FTD Initiative, GENFI.¹

^a*Department of Medical Physics and Biomedical Engineering, University College London, United Kingdom*

^b*Dementia Research Centre, Institute of Neurology, University College London, London WC1N 3BG, United Kingdom*

^c*School of Biomedical Engineering and Imaging Sciences, King's College London, United Kingdom*

^d*Inria Aramis project-team Centre Paris-Rocquencourt, Inserm U 1127, CNRS UMR 7225, Sorbonne Universités, UPMC Univ Paris 06 UMR S 1127, Institut du Cerveau et de la Moelle épinière, ICM, F-75013, Paris, France*

^e*Epione team, Inria Sophia Antipolis, Sophia Antipolis, France*

^f*Department of Medical Statistics, London School of Hygiene & Tropical Medicine, London, United Kingdom*

^g*Erasmus Medical Center, Rotterdam, Netherlands*

^h*University of Brescia*

ⁱ*Dept. of Pathophysiology and Transplantation, "Dino Ferrari" Center, University of Milan, Fondazione C Granda, IRCCS Ospedale Maggiore Policlinico, Milan, Italy*

^j*Cognitive Neurology Research Unit, Sunnybrook Health Sciences Centre; Hurvitz Brain Sciences Research Program, Sunnybrook Research Institute; Department of Medicine, University of Toronto*

^k*Tanz Centre for Research in Neurodegenerative Diseases, University of Toronto*

^l*University of Cambridge*

^m*Karolinska Institutet, Stockholm, Sweden, Karolinska Institutet, Department NVS, Center for Alzheimer Research, Division of Neurogeriatrics, Sweden*

ⁿ*Department of Geriatric Medicine, Karolinska University Hospital, Stockholm, Sweden*

^o*Instituto Neurologico Carlo Besta, Milan, Italy*

^p*IRCCS San Giovanni di Dio Fatebenefratelli Brescia, Italy*

^q*Universit Laval, Quebec, Canada*

^r*University of Western Ontario, Ontario, Canada*

^s*Faculdade de Medicina, Universidade de Lisboa, Portugal*

^t*Department of Neurosciences, Psychology, Drug Research and Child Health (NEUROFARBA), University of Florence, Florence, Italy*

^u*IRCCS Don Gnocchi, Firenze, Italy*

Abstract

Brain atrophy as measured from structural MR images, is one of the primary imaging biomarkers used to track neurodegenerative disease progression. In diseases such as frontotemporal dementia or Alzheimer's disease, atrophy can be observed in key brain

¹List of consortium members in appendix.

structures years before any clinical symptoms are present. Atrophy is most commonly captured as volume change of key structures and the shape changes of these structures are typically not analysed despite being potentially more sensitive than summary volume statistics over the entire structure.

In this paper we propose a spatiotemporal analysis pipeline based on Large Diffeomorphic Deformation Metric Mapping (LDDMM) to detect shape changes from volumetric MRI scans. We applied our framework to a cohort of individuals with genetic variants of frontotemporal dementia and healthy controls from the Genetic FTD Initiative (GENFI) study. Our method, take full advantage of the LDDMM framework, and relies on the creation of a population specific average spatiotemporal trajectory of a relevant brain structure of interest, the thalamus in our case. The residuals from each patient data to the average spatiotemporal trajectory are then clustered and studied to assess when presymptomatic mutation carriers differ from healthy control subjects.

We found statistical differences in shape in the anterior region of the thalamus at least five years before the mutation carrier subjects develop any clinical symptoms. This region of the thalamus has been shown to be predominantly connected to the frontal lobe, consistent with the pattern of cortical atrophy seen in the disease.

Keywords: Shape analysis, clustering, Computational anatomy, thalamus, spatiotemporal geodesic regression, parallel transport

1 Introduction

Neurodegenerative diseases such as frontotemporal dementia (FTD) present progressive symptoms of behavioural and cognitive dysfunction. These changes follow many years of a clinically silent phase in the disease, where abnormal proteins slowly accumulates within the brain, leading to neurodegenerative processes that ultimately result in loss of function. Reliably identifying presymptomatic changes in individuals could lead to intervention with therapies that could slow, or even halt, the onset of these diseases. However, finding a cohort of presymptomatic individuals guaranteed to develop a form of dementia can be challenging. One common strategy is to investigate people who are at-risk for rare autosomal dominant forms of dementia. Half of these individuals are carriers of the mutation, allowing for comparisons between carriers and non-carriers at various stages within the disease process. In the case of genetic FTD, roughly one third of all cases are caused by autosomal dominant mutations, primarily in three genes: chromosome 9 open reading frame 72 (*C9orf72*), progranulin (*GRN*), and microtubule associated protein tau (*MAPT*) [1]. As the name would suggest, in all mutations, there is early involvement of both the frontal and temporal lobes, as well as the insula where differences can be observed as early as ten years before estimated age of expected symptom onset, as shown in Rohrer *et al.* [2]. However, there are additional structures, such as the thalamus, which also appear to be implicated to some degree early on in the disease process [3]. In many forms of FTD, clinical presentations suggest a left/right asymmetry in terms of which hemisphere is more affected, and this is often supported by evidence

22 of increased atrophy within the affected hemisphere [4]. However, the affected side is
23 not consistent across all cases, and in some cases, there is no evidence of an asymmetry.
24 As this asymmetry is likely to start early in the disease process, it must be taken into
25 account when looking to detect early changes with any sensitivity.

26 One biomarker that shows promise during the presymptomatic phase is measurement
27 of atrophy derived from structural magnetic resonance imaging (MRI) [5, 2, 6]. Volumes
28 summarizing change within a region of interest (ROI) tend to be more sensitive to early
29 change than voxelwise approaches, but they do not provide any spatial localisation as
30 to where the atrophy is occurring within the ROI. Conversely, voxelwise analysis can
31 provide better spatial localisation, but the mass univariate nature of the analysis requires
32 correction for multiple comparisons to control for false positive findings, which often
33 results in reduced sensitivity. As loss of brain volume will imply a change in the shape of
34 the structure, a third option is to perform the shape analysis over time for a structure of
35 interest. This could provide more spatial information than a single summary measure of
36 volume alone, but does not require the same level of multiple comparisons as a voxelwise
37 analyses. Given the decades long nature of the disease process, it is not yet feasible
38 to measure the complete time course within one individual. Therefore, the pattern
39 of atrophy over the course of the disease must be estimated through spatiotemporal
40 regression models based on large populations of either cross-sectional data or through
41 longitudinal data that covers a smaller segment (i.e. a few years) of the disease process
42 within each individual.

43 There have been numerous approaches to spatiotemporally model trajectories for age-
44 ing and dementia. Some methods model this evolution using dense 4D deformation fields
45 to measure change between timepoints. Lorenzi *et al.* [7] modelled the 4D deformation
46 fields within a population to obtain subject-specific measurements of atrophy. An ex-
47 tension of this work discriminated spatiotemporal patterns that could be attributed to
48 natural ageing versus those that were related to disease [8]. Other groups establish point
49 correspondences between subjects on a surface representation, and then apply mixed ef-
50 fects models at those points [9, 10, 11], providing fixed effects that represent the change
51 across the overall population while allowing individual longitudinal trajectories as ran-
52 dom effects. More complex representations of surfaces can be used, as in Durrleman
53 *et al.* [12], they proposed a spatiotemporal regression approach to estimate continuous
54 subject-specific trajectories of longitudinal data.

55 In our previous work [13], we defined the shape of the structure of interest as its 3D
56 outline that is rotation and translation invariant. Differences between shapes were quan-
57 tified using the Large Deformation Diffeomorphic Metric Mapping (LDDMM) frame-
58 work [14, 15, 16], producing a smooth and invertible continuum between all possible
59 shapes within the population. The smooth representation of these deformations also
60 acted as low-pass filter, reducing the effects of irregularities and errors in the surface
61 boundaries. Overall, our approach consisted of three main steps. First, using all avail-
62 able data, we compute an average shape spatiotemporal trajectory. Second, for every
63 individual shape we evaluate its distance from the mean trajectory. Last, after spatially
64 normalising all the subject-specific distances to the mean, we run a statistical analysis
65 on the subject-specific residuals to assess when a shape starts diverging from normal-
66 ity. This previous work presented a global spatio-temporal analysis, on one side of the
67 brain, without considering a potential left/right asymmetry of the disease. In this pa-
68 per, we build on the aforementioned framework, which we altered in two main ways.

69 First, we take into consideration the potential asymmetry of FTD by considering the
70 left and right structures using a common shape representation. Second, we modified
71 our feature extraction method using a clustering approach to ensure we can attribute
72 the recovered differences to substructure of the shape under study, and made a novel
73 local analysis, based on clustering of deformations, which takes better advantage of the
74 LDDMM framework.

75 We apply this approach to data from the Genetic FTD Initiative (GENFI), an in-
76 ternational study of autosomal dominant forms of FTD aimed at collecting multimodal
77 neuroimaging, alongside other biomarkers with the objective of obtaining an improved
78 understanding of the changes that are occurring during the presymptomatic phase of
79 the disease. In general, the expected age of onset of clinical symptoms is estimated by
80 using the average age of onset in the family of the subject, allowing to align the different
81 subjects onto a single time axis. We applied our method to a subcortical structure, the
82 thalamus, which has been shown to present volumetric differences before onset in Rohrer
83 *et al.* [2]. We used the expected age to onset to characterise the time progression. In the
84 next section, we will present the different steps of the proposed framework before then
85 further describing the experiment and associated results.

86 2. Method

We indicate with $\{(S_i, t_i)\}_{i \in \{0, \dots, N-1\}}$ a set of N shapes associated with a corre-
sponding time point t_i . With analogy to classical random-effect-modelling approaches,
we assume that each shape is a random realisation of a common underlying spatiotem-
poral process $\phi(t)$:

$$S_i = \rho_i(\phi(B_0, t_i)) + \epsilon_i,$$

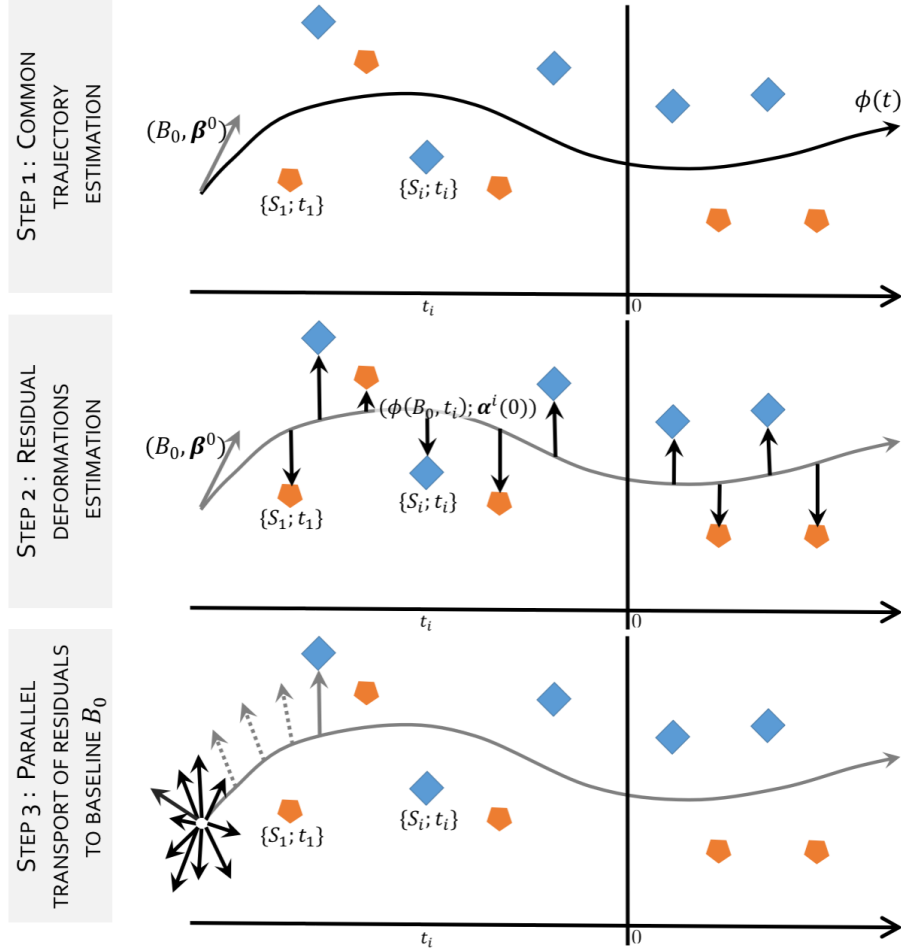
87 where B_0 is a common reference frame, and ρ_i is a subject-specific "residual" defor-
88 mation accounting for individual deviation from the mean shape. We characterise this
89 residual through the diffeomorphism linking the shape S_i to the corresponding sample of
90 the common spatiotemporal trajectory at time point t_i . We also assume that ϵ_i is Gaus-
91 sian randomly distributed noise. In order to identify group-wise differences between the
92 given populations, we rely on the analysis of the subjects-specific residuals deformations
93 ρ_i .

94 This is a challenging problem, since all ρ_i are defined at different time points along
95 the common spatiotemporal trajectory, and therefore cannot be directly compared in a
96 common anatomical framework. Moreover, the optimisation of the functional for the
97 simultaneous estimation of the group-wise trajectory and random effects is not trivial,
98 and would ultimately result in expensive and thus impractical numerical schemes. For
99 these reasons, we propose a serial optimisation of the problem by introducing an efficient
100 numerical framework composed of three steps illustrated in Figure 1.

101 (i) First, we assume that the residuals deformations ρ_i are fixed, and we estimate the
102 common trajectory $\phi(t)$. (ii) Second, given the modelled trajectory ϕ , we estimate the
103 residuals deformations ρ_i through non-linear registration between the trajectory point
104 $\phi(B_0, t_i)$ and S_i . (iii) Third, we spatially normalise the residual deformations in the
105 common initial reference space B_0 using parallel transport.

106 The proposed framework relies on the mathematical setting of the Large Diffeomor-
107 phic Deformation Metric Mapping (LDDMM) framework and the varifold representation

Figure 1: Overview of the proposed regression approach. The temporal axis indicates the time variable attached to the data, in this case the estimated years to expected symptom onset. The residual deformations (step 2) ρ_i parametrised by $(\phi(B_0, t_i); \alpha^i(0))$ computed from the common trajectory (step 1) ϕ parametrised by $(B_0; \beta^0)$, cannot be analysed because they are defined on different spaces i.e. $\phi(B_0, t_i)$. They have to be transported to a common space (i.e. B_0) along the geodesic ϕ , so they can be analysed (step 3).



108 of shapes (section 2.1). This choice allows a mathematically consistent definition of all
 109 steps (section 2.2), namely: (i) the spatiotemporal regression, (ii) the ρ_i deformations
 110 estimation, and (iii) the normalisation of the initial momentum of ρ_i through parallel
 111 transport.

112 *2.1. Large diffeomorphic deformation metric mapping and varifold representation*

113 The LDDMM framework [14, 15] is a mathematical and algorithmic framework based
 114 on flows of diffeomorphisms, which allows comparing anatomical shapes as well as per-
 115 forming statistics. The framework used in this paper is a discrete parametrisation of

116 the LDDMM framework, as proposed by Durrleman *et al.* [17], based on a finite set of
 117 N_{B_0} control points overlaid on the 3D space enclosing the initial shape B_0 . The control
 118 points number and position are independent from the shapes being deformed as they do
 119 not require to be aligned with the shapes' vertices. They are used to define a potentially
 120 infinite-dimensional basis for the parametrization of the deformation. Momentum vec-
 121 tors are associated with the control points and are used as weights for the decomposition
 122 of a given deformation onto this basis.

Deformation maps $\varphi_v : \mathbb{R}^3 \rightarrow \mathbb{R}^3$ are built by integrating time-varying vector fields $(v_t)_{0 \leq t \leq 1}$, such that each $v(\cdot, t)$ belongs to a Reproducing Kernel Hilbert Space (RKHS) V with kernel K_V . We use a Gaussian kernel for all control points x, y :

$$k_V(x, y) = \exp\left(\frac{-|x - y|^2}{\lambda^2}\right) \text{Id},$$

with Id the identity matrix, and λ a scale factor which determines the size of the kernel and therefore the degree of smoothness of the deformations. We define $\varphi_v(x) = \phi_v(x, 1)$ as the diffeomorphism induced by $v(x, t)$ where $\phi_v(x, 1)$ is the unique solution of the differential equation:

$$\frac{d\phi_v}{dt}(x, t) = v(\phi_v(x, t), t), \forall t \in [0, 1] \text{ with } \phi_v(x, 0) = x, \forall x \in \mathbb{R}^3.$$

Velocity fields $v(\cdot, t)$ are controlled via an energy functional $\int_0^1 \|v(\cdot, t)\|_V^2 dt$, where $\|\cdot\|_V$ is a Hilbert norm defined on vector fields of \mathbb{R}^3 , which is used as a regularity term in the matching functional to penalise non-regularity. In the LDDMM framework, matching two shapes S and T requires estimating an optimal deformation map $\phi : \mathbb{R}^3 \rightarrow \mathbb{R}^3$ such that $\phi(S)$ is close to T . This is achieved by optimising

$$d([\varphi_v(S)], [T])^2 + \gamma \int_0^1 \|v(\cdot, t)\|_V^2 dt,$$

123 where γ balances the regularity of ϕ_v against the spatial proximity d , a similarity measure
 124 between the varifold representation of $\varphi_v(S)$ and T noted respectively $[\varphi_v(S)]$ and $[T]$.

In a discrete setting, the vector fields $v(x, t)$ corresponding to optimal maps are expressed as combinations of spline parametrised fields that involve the reproducing kernel K_V of the space V :

$$v(x, t) = \sum_{p=1}^{N_{B_0}} K_V(x, x_p(t)) \alpha_p(t),$$

125 where $x_p(t) = \phi_v(x_p, t)$ are the trajectories of control points x_p . The control points
 126 are regularly spaced on a 3D grid overlaid on the space that contains the mesh of the
 127 subject S . The control point spacing is defined by the size of the kernel K_V . The
 128 time-dependent vectors $\alpha_p(t) \in \mathbb{R}^3$ are referred to as momentum vectors attached to x_p .
 129 The full deformation can be encoded by the set of initial momentum vectors $\alpha(0) =$
 130 $\{\alpha_p(0)\}_{1 \leq p \leq n}$ located at the points $\{x_p\}_{1 \leq p \leq n}$. This allows the analysis of a set of
 131 deformation maps from a given template to the observed shapes by performing statistics
 132 on the initial momentum vectors defined on control points located around the template

133 shape. The process of generating back any deformation map from initial conditions
 134 $(x_p(0), \alpha_p(0))$, i.e. integrating the geodesic equations, is called geodesic shooting or
 135 exponential map and is noted $\exp_{x_p(0)}(\alpha_p(0))$.

136 As previously stated, varifolds are used to represent shapes [18]. They are non-
 137 oriented versions of the representation with currents [19], which are used to efficiently
 138 model a large range of shapes. To represent a shape S as a varifold, the shape space
 139 is embedded into the dual space of a RKHS W , noted W^* , and encoded using a set
 140 of non-oriented unit normals attached on each vertex of the shape. This kernel-based
 141 embedding allows to define a distance between different embedded shapes. Varifolds are
 142 robust to varying topologies, do not require point to point correspondences, and embed
 143 the shapes in a vector space, which facilitate the interpretation of results. The varifold
 144 representation of a discretised mesh composed by M triangles S is noted $[S]$ and writes:
 145 $[S](\omega) = \sum_{k=1}^M \omega(c_k) \tau(c_k)^2 / \|\tau(c_k)\|$ with ω a vector field in W , c_k the centre of the
 146 triangle k , and $\tau(c_k)$ the tangent of the surface S at point c_k .

147 2.2. Residual extraction framework

148 Due to the asymmetry of the disease, the proposed framework has been designed so
 149 that it is unbiased to the affected side. For each subject, rather than considering the left
 150 or right structure, we build a mean shape by averaging both sides. First, the structure
 151 of interest is segmented using the method proposed by Cardoso *et al.* [20]. Second, we
 152 flip all input T1w brain images and segmentation masks, in order to have all structures,
 153 left and right, on the same side. Third, we affinely align the T1w brain images (the
 154 originals and the flipped ones) to a subject-specific mid-space [21]. The MNI52 atlas
 155 was used to define the mid-space and ensure that all subjects have a similar total intra-
 156 cranial volume (TIV). TIV varies from subject to subject due to normal variability in
 157 the population. Alignment to a common mid-space enables to discard this inter-subject
 158 variability through normalisation. The obtained affine transformations are then applied
 159 to the corresponding segmentation masks. Fourth, we compute a mask covering the
 160 area of the structure of interest and its surroundings for all T1w MRI, to estimate a
 161 rigid refinement focused on the area of interest. This is achieved by a 6-voxel dilation
 162 of the union of all propagated masks to ensure that for each subject, the structure of
 163 interest and its surrounding are considered. The rigid refinement step is done using the
 164 T1w MRIs rather than the segmented shape. Finally, we extract the meshes of the left
 165 (flipped, L_i) and right structures (R_i), and compute the mean shape, by estimating the
 166 diffeomorphisms $\chi_v^{(i)}$ for each subject i , such as $\chi_v^{(i)} = \operatorname{argmin}_{\frac{1}{2}(\|\chi_{v_i}(L_i) - [S_i]\|_{W^*}^2 +$
 167 $\|\chi_{v_i}(R_i) - [S_i]\|_{W^*}^2) + \gamma \int_0^1 \|v_i(\cdot, t)\|_V^2 dt$ with W^* the space of varifolds and S_i , the
 168 obtained subject-specific average shape of the structure of interest, is associated with a
 169 temporal information t_i , the number of years to the expected onset (EYO) of the subject
 170 i .

171 The computation of the spatiotemporal regression [12] requires an initial shape $B_0 =$
 172 $\{x_p\}_{p=1, \dots, N_{B_0}}$ as reference. To avoid any bias towards a subject selected as the initial
 173 shape, we estimate the initial shape from the 10 subjects who are the furthest away from
 174 expected symptom onset, who are all approximately 40 years before their expected onset
 175 of clinical symptoms according to EYO. We estimate the centroid of those 10 subjects
 176 using the diffeomorphic Iterative Centroid method [22], which estimates a centre of a
 177 given population in a reasonable computation time [23].

The spatiotemporal regression of the set of shapes $\{(S_i, t_i)\}_{i \in \{0; \dots; N-1\}}$ is implemented in the Deformetrica software [24, 25]². The EYO values are discretised into T time points. Starting from B_0 at time $t = 0$, a geodesic moving through the positions $\phi(B_0, t)$, $\forall t \in \{0; \dots; T\}$ is computed by minimising the discrepancy between the model at time t (i.e. $\phi(B_0, t)$) and the observed shapes S_i :

$$E(\phi_v) = \sum_{t_i} d([\phi_v(B_0, t_i)], [S_i])^2 + \gamma \|v\|_{V\phi}^2,$$

178 with v the time-varying velocity vector field that belongs to the RKHS V determined by
 179 the Gaussian Kernel K_V . The initial momentum vectors $\beta^0(0) = \{\beta_p^0(0)\}_{1 \leq p \leq N_{B_0}}$ are
 180 defined on the control points grid overlaid on the baseline shape B_0 and fully encode the
 181 geodesic regression parametrised by $\{B_0; \beta^0(0)\}$.

182 We then compute the residuals diffeomorphic deformations ρ_i between every obser-
 183 vation and the spatio-temporal average shape by estimating a geodesic between $\phi(B_0, t_i)$
 184 and $\{S_i, t_i\}$. This yields a set of trajectories parametrised by $\{\phi(B_0, t_i); \alpha^i(0)\}_{i \in \{0; \dots; N-1\}}$
 185 that encode the deformations ρ_i from the spatio-temporal regression to all subjects, with
 186 $\alpha^i(0)$ the initial momentum vectors, where the varying parameter is the step of the de-
 187 formation. This parameter should not be confused with the time variable corresponding
 188 to the EYO and to the time varying deformation of the main spatio-temporal trajectory.

189

In order to be able to compare this set of momenta, we gather them in the same Euclidean space. This is achieved by transporting all momenta into the initial space of $B_0 = \phi(B_0, 0)$, using a parallel transport method based on Jacobi fields as introduced in [26]. Parallel transporting a vector along a curve (the computed trajectory parametrised by $(B_0; \beta^0(0))$) consists in translating it across the tangent spaces along the curve by preserving its parallelism, according to a given connection. The Levi-Civita connection is used in the LDDMM framework. The vector is parallel transported along the curve if the connection is null for all steps along the curve [27]. We use Jacobi field instead of the Schild's Ladder method [28], to avoid the cumulative errors and the excessive computation time due to the computation of Riemannian Logarithms in the LDDMM framework, required for the Schild's Ladder. The cumulative errors would have differed from subject to subject and thus introduce a bias. Indeed, their distances from the baseline shape vary, as they all are at different points along the temporal axis. The Jacobi field, used to transport a vector $\alpha^i(0)$ from a time t to the time $t_0 = 0$ along the geodesic γ , is defined as:

$$J_{\gamma(t)}(0, -\beta^0(t), \alpha_i(0)) = \frac{\partial}{\partial \epsilon} \exp_{\gamma(t)}(1/T(-\beta^0(t) + \epsilon \alpha_i(0))).$$

190 The transported initial momentum vector $\alpha_i(0)$ is noted $\theta_i(0)$. After parallel transport-
 191 ing all residuals, all initial momentum vectors are defined in B_0 .

192 2.3. Feature extraction for statistical analysis

193 Each transported initial momentum vectors $\theta_i(0)$ is of size $3 \times N_{B_0}$, where N_{B_0} is the
 194 number of control point used to parametrise the geodesics.

²<http://www.deformetrica.org/>

195 Jacobian determinants are a geometric measure derived from the full deformation
196 tensor that is commonly used to study shrinkage or growth of the surface. In this work
197 we propose an analysis framework where we decouple the amplitude and the orientation
198 of the deformation. Such an approach will still analyse growth and shrinkage, but also
199 other geometric aspects, such as rotation and torsion, that are not captured by the
200 surface Jacobian. Furthermore, the changes being analysed are residual deformations,
201 which are defined using a purely geometrical spatio-temporal regression. As such, the
202 shape differences that we aim to detect are not necessarily limited to shrinkage or growth,
203 but can be induced by more complex effects.

204 To analyse direct measures from deformation and to avoid losing statistical power
205 from doing a large number of comparisons, we propose an original clustering approach
206 by grouping the parametrisation $(B_0; \beta^0(0))$ of the spatio-temporal regression ϕ into
207 clusters.

208 To do so, we defined a similarity measure derived from the positions of the control
209 points x_p , the pairwise angles and the magnitudes of the initial momentum vectors
210 $\{\beta_p^0(0)\}_{1 \leq p \leq N_{B_0}}$ attached to the control point x_p . The difference between two control
211 points x_p and $x_q \forall p, q \in \{1; \dots; N_{B_0}\}$ is defined by the euclidean distance, the angle be-
212 tween two vectors is defined by the cosine. The similarity between p and q is defined by
213 $s(p, q) = -5\|x_p - x_q\|^2 + 2(\cos(\beta_p^0, \beta_q^0) + 1) - \|\beta_p^0\|^2 - \|\beta_q^0\|^2$. Parameters are chosen
214 to balance between vector similarity and control point positions and depend on the dis-
215 tance in mm between two points. The distance is determined by the kernel K_V so that
216 clusters encompass control points and their momentum vectors within the same area and
217 look alike. To estimate those clusters, we used a spectral clustering method [29] using
218 the discretisation approach presented in [30] for initialisation, as it has been shown to
219 be more stable than other approaches such as k-means for initialisation. 3000 different
220 initialisations are generated and we select the best one in term of inertia for spectral
221 clustering. We chose 10 clusters as thought this would be a good balance between re-
222 ducing the number of multiple comparisons while maintaining some spatial specificity in
223 the analyses and equitable clusters. A mean vector is then computed from the parallel
224 transported residuals defined on the control points of the cluster. This is done for each
225 cluster and for each subject. We then obtain N vectors $\{\nu_{i,k}\}$ per cluster k , and 10
226 vectors per subject i .

227 For the statistical analysis, we will use two uncorrelated descriptors for the vectors
228 $\{\nu_{i,k}\}$: the amplitude and the orientation. The orientation of the vectors $\{\nu_{i,k}\}$ is origi-
229 nally represented by 3 angles, one per axis. The angles are then projected via a Principal
230 Component Analysis onto the first eigenvector, therefore the orientation of $\{\nu_{i,k}\}$ con-
231 sidered here is represented by one continuous scalar, leading to the set of responsive
232 variables $\{O_{i,k}\}$.

233 3. Data and application

234 As previously mentioned, we applied the proposed framework to the GENFI study
235 and used the thalamus as structure of interest.

236 3.1. Dataset description

237 All participants included in this study come from the data freeze 1 of the GENFI
238 cohort described in detail in [2]. Initial results from this cohort [2] show volumetric

Table 1: Data demographics, in absolute values.

	Non-carriers n=98	Mutation carriers n=113
Males	59	56
Asymptomatic	98	76
Age in years (med (IQR))	50.2 (62.1 - 36.6=25.5)	52.7 (62.7 - 41.1=21.6)
Years from expected onset:		
≤ -20 years	30	21
$-20 \leq \text{years} \leq -10$	16	21
$-10 \leq \text{years} < 0$	23	22
$0 \leq \text{years}$	29	49

239 differences in the thalamus at least 5 years before expected age of onset with an effect in
240 all genetic subtypes, and so we chose this well-defined subcortical structure for further
241 analysis. In this paper we used 211 participants, 113 mutation carriers (MAPT=26,
242 GRN=53, C9ORF=34) and 98 non-carriers. All participants have a T1-weighted (T1w)
243 MRI available and an associated expected years to symptom onset (EYO). The EYO,
244 ranging from -40 years to +20 years, is calculated as the difference between the age of
245 the participant at the time of the T1w acquisition and the mean age at onset of affected
246 family members, as in [2]. The median of the age at onset of all subjects is 59.7 years
247 with inter-quartile range $IQR = 60.5 - 55$. Table 1 shows the demographics of the study
248 participants used in this analysis.

249 3.2. Application to the thalamus

250 As previously mentioned in section 2.2, all T1w MRIs and associated segmentations of
251 the structure of interest, the thalamus, are first aligned to a common space. This enables
252 to normalise for intra-cranial volume differences across subjects. We then extracted
253 the meshes corresponding to the thalamus, composed by around 2,300 vertices. This
254 resulted in 211 thalamus meshes, representing the mean left and the right shape. Each
255 were associated with the EYO of the corresponding subject as well as mutation status:
256 non-carrier and mutation carrier (MC). For the spatio-temporal regression, we used 30
257 time points, which corresponds approximately to one time point every two years. The
258 space of deformations V was defined using a 11mm width kernel, approximately half of
259 the length of the thalamus, which leads to a set of 288 control points. For the space of
260 varifolds we used a 5mm width kernel which covers the size of 2 voxels. This parameter
261 was fixed and thought to be a good compromise between the capture of high frequency
262 changes and the robustness of the approach to noise in the shape segmentation.

263 Similarly to the volumetric analysis performed by Rohrer *et al.* [2], we used a mixed
264 effect model to study the shape difference between the non-carriers and mutation carriers.
265 Amplitude $\{|\nu_{i,k}|\}$ and orientation $\{O_{i,k}\}$ were used as responsive variables and the fixed
266 effects predictors of interest were mutation carrier status, EYO, interaction between
267 mutation carrier status and EYO, sex and the site in which the subject has been scanned.
268 A random intercept for family allows values of the marker to be correlated between
269 family members. Correcting for age of subjects is not relevant here, since there is a strong
270 correlation ($r = 0.9$) between EYO and age.

Table 2: p-values with the corresponding χ^2 value, resulting from the Wald tests testing the mutation carrier (MC) differences (test T1), and the evolution of those differences along time (test T2), for the amplitude of the initial momentum vector and its orientation, for the clusters showing at least one significant test. Bold p-values: ≤ 0.05 , and starred (*) p-values indicate the corrected threshold for multiple comparisons: $\leq 2.5e-3$.

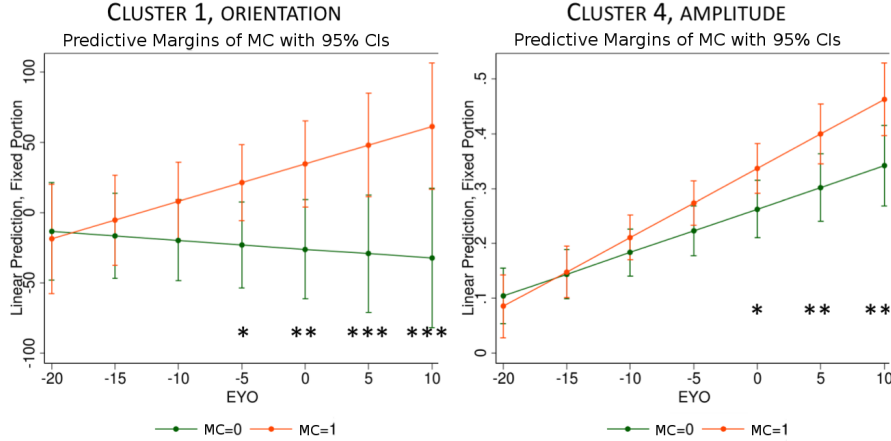
		C1	C2	C4	C6	C7
Ampl.	T1	$p = 0.48$	$p = 0.51$	$p = \mathbf{1.5e-3 (*)}$	$p = 0.08$	$p = 0.76$
		$\chi_{df=2}^2 = 1.43$	$\chi_{df=2}^2 = 1.35$	$\chi_{df=2}^2 = 12.94$	$\chi_{df=2}^2 = 5.10$	$\chi_{df=2}^2 = 0.55$
	T2	$p = 0.24$	$p = 0.26$	$p = \mathbf{1.5e-3 (*)}$	$p = \mathbf{0.04}$	$p = 0.68$
		$\chi_{df=1}^2 = 1.37$	$\chi_{df=1}^2 = 1.28$	$\chi_{df=1}^2 = 10.08$	$\chi_{df=1}^2 = 4.20$	$\chi_{df=1}^2 = 0.17$
Orient.	T1	$p = \mathbf{2e-4 (*)}$	$p = 0.12$	$p = 0.85$	$p = 0.63$	$p = 0.08$
		$\chi_{df=2}^2 = 16.60$	$\chi_{df=2}^2 = 4.17$	$\chi_{df=2}^2 = 0.33$	$\chi_{df=2}^2 = 0.92$	$\chi_{df=2}^2 = 5.06$
	T2	$p = \mathbf{9e-4 (*)}$	$p = \mathbf{0.05}$	$p = 0.62$	$p = 0.34$	$p = \mathbf{0.04}$
		$\chi_{df=1}^2 = 11.01$	$\chi_{df=1}^2 = 3.85$	$\chi_{df=1}^2 = 0.25$	$\chi_{df=1}^2 = 0.91$	$\chi_{df=1}^2 = 4.29$

271 We performed a Wald test for every model, assessing the difference between the
272 mutation carrier group and the non-carrier group, and the evolution of differences across
273 time. For each analysis with statistically significant differences between both groups,
274 further Wald tests were conducted every 5 years as in the volumetric analysis [2] to
275 assess how long before the expected onset we could detect changes between mutation
276 carriers and controls.

277 4. Results

278 Results for the amplitude and the orientation of the residual momentum vectors
279 are presented in Table 2. We found significant differences, after correction for multiple
280 comparisons, in cluster 1 and cluster 4, for both tests; T1: differences between MC and
281 controls and T2: differences over time between MC and controls. Those differences
282 are significant after Bonferroni correction for multiple comparisons (20 tests). Cluster
283 1 shows differences in the orientation, and no differences in the amplitude, whereas
284 cluster 4 shows significant differences for those 2 tests in amplitude, and no differences
285 in orientation. Those 2 clusters are thus selected for the next Wald test step. Wald
286 tests were conducted every 5 years between 20 years before the expected onset and 10
287 years after the expected onset to limit the number of tests, since we would not expect
288 substantial changes in volume or shape 20 years before onset. Results are shown in
289 Figure 2, the p-values and confidence intervals are corrected for multiple comparison
290 across time using Bonferroni correction. The orientation of the cluster 1 deformation
291 shows significant differences between the mutation carriers and controls, 5 years before
292 EYO ($p = 0.03$), the uncorrected for this cluster is $p = 2e-3$, to keep a head to head
293 comparison with the previous studies on this dataset [2, 13] in which the p-values at -5
294 EYO was significant but higher than here. The uncorrected p-values show significant
295 differences at 10 years before EYO, with $p=0.048$ for the orientation of cluster 1. The
296 amplitude between the two groups doesn't differ significantly for the cluster 4 before
297 EYO for corrected p-values, and differs 5 years before onset without correction ($p=0.05$).

Figure 2: cluster 1 (orientation component) and cluster 4 (amplitude component) estimates in mutation carriers and controls, by estimated time from expected symptoms onset (EYO). p-values and confident interval are Bonferroni corrected. * : $p < 0.05$, ** : $p < 0.01$, *** : $p < 0.001$



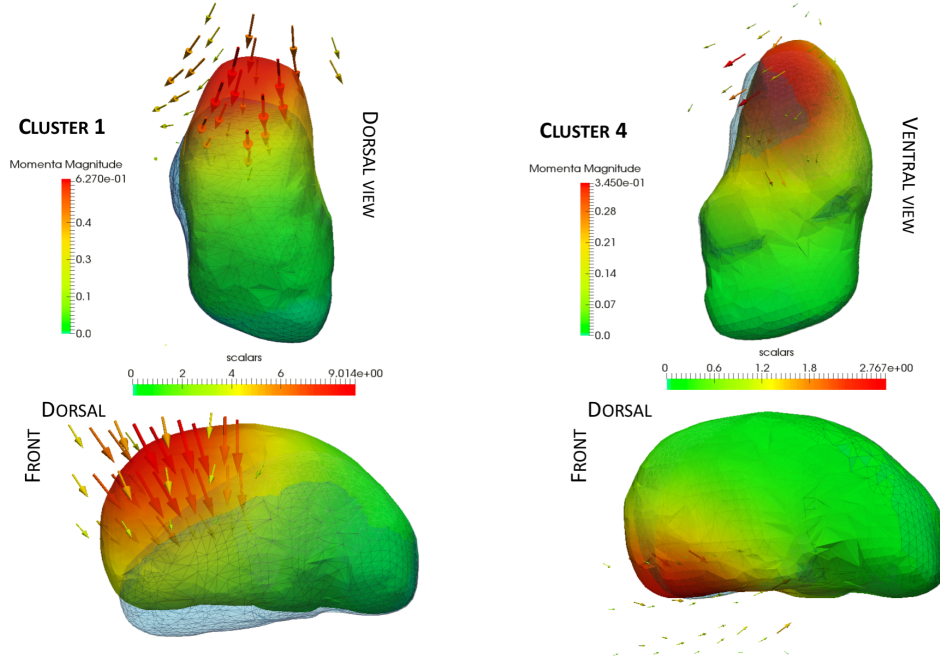
298 Figure 3 shows the initial momentum vectors of clusters 1 and 4, and the amount of
 299 displacement due to the deformations corresponding to those clusters 1 and 4, where
 300 each cluster has its own colour scale, since the maximum displacement for cluster 4 is
 301 about 3 mm, against 9 mm for cluster 1. Deformations affect more the anterior part of
 302 the thalamus.

303 Since the number of clusters used (i.e. 10), is an arbitrary choice, we tried to reproduce
 304 the results with different number of clusters. We performed the analysis for 2, 4, 6,
 305 8, 10, 12, 14 and 16 clusters which results can be found in supplementary material
 306 (<https://zenodo.org/record/1324234>). For 6 clusters and 16 clusters, there were
 307 differences in orientation for one of the clusters which deformation corresponds to the
 308 one of cluster 1 (see Figure 3). From 8 clusters to 14 clusters, we found a cluster with
 309 strong differences 5 years before the expected onset ($p < 0.01$) in orientation whose
 310 deformation corresponds again to the one of the cluster 1 ($p = 0.003$). The change
 311 in orientation for the deformation recovered within cluster 1 (see Figure 3) appears to
 312 be stable for different clustering of the parametrisation of the global spatiotemporal
 313 trajectory (<https://zenodo.org/record/1324234>, Figure 1).

314 5. Discussion and conclusion

315 We applied a novel method of statistical shape analysis to a cohort of individuals with
 316 genetic FTD in order to localise any presymptomatic differences present in the shape of
 317 the thalamus. From the analysis, we conclude that differences are observed five years
 318 before expected symptom onset. While volumetric analysis [2] and our initial shape
 319 analysis [13] also found these changes, this method showed significance that survived
 320 correction for multiple comparisons. The change in shape is primarily attributable to
 321 differences in orientation of the deformation rather than changes in amplitude of the

Figure 3: Deformation obtained by the momentum vectors (displayed here and coloured by amplitude) of Cluster 1 and Cluster 4. The colour map is in millimetres and indicates the displacement due to the corresponding deformation (blue meshes). The scale for Cluster 1 range from 0 mm to 9 mm, and from 0 mm to 2.8 mm for Cluster 4.

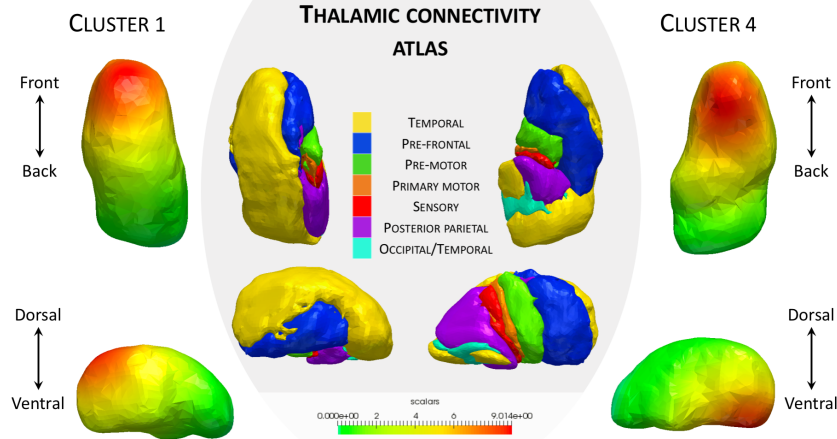


322 deformation, which would imply a simple scaling effect of the region. This result confirms our previous shape analysis in this cohort [13] that was performed at a global level
 323 through a kernel principal component analysis. The first mode of variation which detected significant shape differences around the same point with respect to EYO did not
 324 capture volume differences but only changes in the orientation of the deformation. The results of those studies seem to indicate that shape changes occur before volume changes.
 325
 326
 327

328 The regions of the thalamus most affected in the analysis are anterior, overlapping with the anterior nuclei group. The main connections of these nuclei are to the pre-
 329 frontal cortices, an area universally affected in all genetic forms of FTD. To illustrate this purpose, we used the Oxford thalamic connectivity atlas, a thalamic atlas based on
 330 its anatomical connectivity to the cerebral cortex [31], and displayed at Figure 4 the atlas next to the clusters 1 and 4. Whilst differences are seen in cortical involvement within
 331 the different genetic forms of FTD [32], it may well be that this joint analysis of GRN, C9orf72 and MAPT mutations is only identifying thalamic regions jointly affected.
 332
 333
 334
 335

336 This approach could also be used to explore other regions known to be implicated in FTD, such as the insular cortex, which is located in the lateral sulci and is connected
 337 to the limbic system, and to the thalamus. In fact, it would be interesting to analyse the insula and thalamus together, and the insula only, so we could investigate if shape
 338 changes in both structures are linked.
 339
 340

Figure 4: Thalamic connectivity atlas, and deformations clusters 1 and 4. The orientation of cluster 1 leads to significant differences between MC and controls 5 years before EYO.



341 The small numbers in each group precluded any analysis of the individual genetic
 342 types, but it will be important to investigate future data freezes from the GENFI study
 343 with larger numbers, particularly the C9orf72 group who have been shown to have early
 344 thalamic involvement [32].

345 Future studies should also evaluate the initial momentum vectors of individual geodesic
 346 evolution of shapes from each subject, through longitudinal data. Those individual evo-
 347 lutions would provide information on the differences of evolutions of shape between the
 348 mutation carriers and the controls.

349 Acknowledgements

350 Claire Cury is supported by the EU-FP7 project VPH-DARE@IT (FP7-ICT-2011-
 351 9-601055). Stanley Durrleman has received funding from the program Investissements
 352 d'avenir ANR-10-IAIHU-06 and the European Unions Horizon 2020 research and inno-
 353 vation programme EuroPOND under grant agreement No 666992, and is funded by the
 354 European Research Council (ERC) under grant agreement No 678304. Marco Lorenzi re-
 355 ceived funding from the EPSRC (EP/J020990/1). Jennifer Nicholas is supported by UK
 356 Medical Research Council (grant MR/M023664/1). David Cash is supported by grants
 357 from the Alzheimer Society (AS-PG-15-025), Alzheimers Research UK (ARUK-PG2014-
 358 1946) and Medical Research Council UK (MR/M023664/1). JBR is supported by the
 359 Wellcome Trust (103838). Jonathan D. Rohrer is an MRC Clinician Scientist and has
 360 received funding from the NIHR Rare Diseases Translational Research Collaboration. Se-
 361 bastien Ourselin receives funding from the EPSRC (EP/H046410/1, EP/K005278), the
 362 MRC (MR/J01107X/1), the NIHR Biomedical Research Unit (Dementia) at UCL and the
 363 National Institute for Health Research University College London Hospitals Biomedical
 364 Research Centre (NIHR BRC UCLH/UCL High Impact Initiative- BW.mn.BRC10269).
 365 Marc Modat is supported by the UCL Leonard Wolfson Experimental Neurology Centre

366 (PR/ylr/18575) and Alzheimers Society UK (AS-PG-15-025). We would like to thank
367 the participants and their families for taking part in the GENFI study.

368 References

- 369 [1] J. D. Rohrer, J. D. Warren, Phenotypic signatures of genetic frontotemporal dementia:, Current
370 Opinion in Neurology 24 (6) (2011) 542–549. doi:10.1097/WC0.0b013e32834cd442.
- 371 [2] J. D. Rohrer, J. M. Nicholas, D. M. Cash, J. van Swieten, E. Dopper, L. Jiskoot, R. van Minkelen,
372 S. A. Rombouts, M. J. Cardoso, S. Clegg, M. Espak, S. Mead, D. L. Thomas, E. D. Vita, et al.,
373 Presymptomatic cognitive and neuroanatomical changes in genetic frontotemporal dementia in the
374 Genetic Frontotemporal dementia Initiative(GENFI) study: a cross-sectional analysis, The Lancet
375 Neurology 14 (3) (2015) 253–262. doi:10.1016/S1474-4422(14)70324-2.
- 376 [3] M. Bocchetta, E. Gordon, M. J. Cardoso, M. Modat, S. Ourselin, J. D. Rohrer,
377 Thalamic atrophy in frontotemporal dementia - Not just a C9orf72 problem, NeuroImage: Clinical.
378 [4] M. Boccardi, L. Bresciani, C. Geroldi, A. Beltramello, G. B. Frisoni, M. P. Laakso, Clinical charac-
379 teristics of frontotemporal patients with symmetric brain atrophy, European Archives of Psychiatry
380 and Clinical Neuroscience 252 (5) (2002) 235–239. doi:10.1007/s00406-002-0388-z.
- 381 [5] T. L. S. Benzinger, T. Blazey, C. R. Jack, et al., Regional variability of imaging biomarkers in
382 autosomal dominant Alzheimer’s disease., Proceedings of the National Academy of Sciences 110 (47)
383 (2013) E4502–9.
- 384 [6] J. M. Schott, J. W. Bartlett, N. C. Fox, J. Barnes, Increased brain atrophy rates in cognitively
385 normal older adults with low cerebrospinal fluid A β 1-42., Annals of neurology 68 (6) (2010) 825–
386 34. doi:10.1002/ana.22315.
387 URL <http://www.ncbi.nlm.nih.gov/pubmed/21181717>
- 388 [7] M. Lorenzi, N. Ayache, G. Frisoni, X. Pennec, et al., 4D registration of serial brain’s MR images: a
389 robust measure of changes applied to Alzheimer’s disease, in: MICCAI Workshop, Spatio Temporal
390 Image Analysis Workshop (STIA), 2010.
- 391 [8] M. Lorenzi, X. Pennec, G. B. Frisoni, N. Ayache, Disentangling normal aging from Alzheimer’s
392 disease in structural magnetic resonance images, Neurobiology of Aging 36 (2015) S42–S52. doi:
393 10.1016/j.neurobiolaging.2014.07.046.
- 394 [9] M. Datar, P. Muralidharan, A. Kumar, S. Gouttard, J. Piven, G. Gerig, R. Whitaker, P. T. Fletcher,
395 Mixed-Effects Shape Models for Estimating Longitudinal Changes in Anatomy, in: D. Hutchi-
396 son, T. Kanade, J. Kittler, J. M. Kleinberg, F. Mattern, J. C. Mitchell, M. Naor, O. Nierstrasz,
397 C. Pandu Rangan, B. Steffen, M. Sudan, D. Terzopoulos, D. Tygar, M. Y. Vardi, G. Weikum,
398 S. Durrleman, T. Fletcher, G. Gerig, M. Niethammer (Eds.), Spatio-temporal Image Analysis for
399 Longitudinal and Time-Series Image Data, Vol. 7570, Springer Berlin Heidelberg, Berlin, Heidel-
400 berg, 2012, pp. 76–87.
- 401 [10] P. Muralidharan, J. Fishbaugh, H. J. Johnson, S. Durrleman, J. S. Paulsen, G. Gerig, P. T.
402 Fletcher, Diffeomorphic Shape Trajectories for Improved Longitudinal Segmentation and Statistics,
403 in: P. Golland, N. Hata, C. Barillot, J. Hornegger, R. Howe (Eds.), Medical Image Computing and
404 Computer-Assisted Intervention ??? MICCAI 2014, Vol. 8675, Springer International Publishing,
405 2014, pp. 49–56.
- 406 [11] L. Younes, M. Albert, M. I. Miller, B. R. Team, et al., Inferring changepoint times of medial temporal
407 lobe morphometric change in preclinical alzheimer’s disease, NeuroImage: Clinical 5 (2014) 178–187.
- 408 [12] S. Durrleman, X. Pennec, A. Trouvé, J. Braga, G. Gerig, N. Ayache, Toward a comprehensive
409 framework for the spatiotemporal statistical analysis of longitudinal shape datas, International
410 Journal of Computer Vision 103 (1) (2013) 22–59. doi:10.1007/s11263-012-0592-x.
- 411 [13] C. Cury, M. Lorenzi, D. Cash, J. M. Nicholas, A. Routier, J. Rohrer, S. Ourselin, S. Durrleman,
412 M. Modat, Spatio-Temporal Shape Analysis of Cross-Sectional Data for Detection of Early Changes
413 in Neurodegenerative Disease, in: M. Reuter, C. Wachinger, H. Lombaert (Eds.), Spectral and
414 Shape Analysis in Medical Imaging, Vol. 10126, Springer International Publishing, 2016, pp. 63–75.
415 doi:10.1007/978-3-319-51237-2_6.
416 URL http://link.springer.com/10.1007/978-3-319-51237-2_6
- 417 [14] A. Trouvé, Diffeomorphisms groups and pattern matching in image analysis, International Journal
418 of Computer Vision 28 (3) (1998) 213–221.
- 419 [15] M. F. Beg, M. I. Miller, A. Trouvé, L. Younes, Computing large deformation metric mappings via
420 geodesic flows of diffeomorphisms, International Journal of Computer Vision 61 (2) (2005) 139–157.

- 421 [16] J. Glaunès, A. Qiu, M. I. Miller, L. Younes, Large Deformation Diffeomorphic Metric Curve Map-
422 ping, *International Journal of Computer Vision* 80 (3) (2008) 317–336.
- 423 [17] S. Durrleman, M. Prastawa, G. Gerig, S. Joshi, Optimal Data-Driven Sparse Parameterization of
424 Diffeomorphisms for Population Analysis, in: D. Hutchison, T. Kanade, J. Kittler, J. M. Kleinberg,
425 F. Mattern, J. C. Mitchell, M. Naor, O. Nierstrasz, C. Pandu Rangan, B. Steffen, M. Sudan,
426 D. Terzopoulos, D. Tygar, M. Y. Vardi, G. Weikum, G. Székely, H. K. Hahn (Eds.), *Information*
427 *Processing in Medical Imaging*, Vol. 6801, Springer Berlin Heidelberg, Berlin, Heidelberg, 2011, pp.
428 123–134.
- 429 [18] N. Charon, A. Trounev, The Varifold Representation of Nonoriented Shapes for Diffeomorphic Reg-
430 istration, *SIAM Journal on Imaging Sciences* 6 (4) (2013) 2547–2580. doi:10.1137/130918885.
- 431 [19] M. Vaillant, J. Glaunès, Surface matching via currents, in: G. E. Christensen, M. Sonka (Eds.), *In-*
432 *formation Processing in Medical Imaging*, Vol. 3565 of *Lecture Notes in Computer Science*, Springer
433 Berlin Heidelberg, 2005, pp. 381–392.
- 434 [20] M. J. Cardoso, K. Leung, M. Modat, S. Keihaninejad, D. Cash, J. Barnes, N. C. Fox, S. Ourselin, for
435 ADNI, STEPS: Similarity and truth estimation for propagated segmentations and its application to
436 hippocampal segmentation and brain parcellation., *Medical Image Analysis* 17 (6) (2013) 671–684.
- 437 [21] M. Modat, D. M. Cash, P. Daga, G. P. Winston, J. S. Duncan, S. Ourselin, Global image registration
438 using a symmetric block-matching approach, *Journal of Medical Imaging* 1 (2) (2014) 024003–
439 024003.
- 440 [22] C. Cury, J. A. Glaunès, O. Colliot, Diffeomorphic iterative centroid methods for template esti-
441 mation on large datasets, in: F. Nielsen (Ed.), *Geometric Theory of Information, Signals and*
442 *Communication Technology*, Springer International Publishing, 2014, pp. 273–299.
- 443 [23] C. Cury, J. A. Glaunès, R. Toro, M. Chupin, G. Schumann, V. Frouin, J.-B. Poline, O. Colliot, the
444 Imagen Consortium, Statistical Shape Analysis of Large Datasets Based on Diffeomorphic Iterative
445 Centroids, *Frontiers in Neuroscience* 12 (2018) 803. doi:10.3389/fnins.2018.00803.
446 URL <https://www.frontiersin.org/article/10.3389/fnins.2018.00803/full>
- 447 [24] S. Durrleman, M. Prastawa, N. Charon, J. R. Korenberg, S. Joshi, G. Gerig, A. Trounev, Morphom-
448 etry of anatomical shape complexes with dense deformations and sparse parameters, *NeuroImage*
449 101 (0) (2014) 35 – 49. doi:http://dx.doi.org/10.1016/j.neuroimage.2014.06.043.
- 450 [25] A. Routier, P. Gori, A. B. G. Fouquier, S. Lecomte, O. Colliot, S. Durrleman, Evaluation of mor-
451 phometric descriptors of deep brain structures for the automatic classification of patients with
452 Alzheimer’s disease, mild cognitive impairment and elderly controls, in: *MICCAI Workshop, Chal-*
453 *lenge on Computer-Aided Diagnosis of Dementia Based on Structural MRI Data*, 2014.
- 454 [26] L. Younes, Jacobi fields in groups of diffeomorphisms and applications, *Quarterly of applied math-*
455 *ematics* 65 (2007) 113–134.
- 456 [27] M. Lorenzi, X. Pennec, Efficient Parallel Transport of Deformations in Time Series of Images: From
457 Schild’s to Pole Ladder, *Journal of Mathematical Imaging and Vision* 50 (1-2) (2013) 5–17.
- 458 [28] A. Kheyfets, W. A. Miller, G. A. Newton, Schild’s Ladder Parallel Transport Procedure for an
459 Arbitrary Connection, *International Journal of Theoretical Physics* 39 (12) (2000) 2891–2898. doi:
460 10.1023/A:1026473418439.
- 461 [29] U. von Luxburg, A Tutorial on Spectral Clustering (Nov. 2007).
- 462 [30] S. Y. Jianbo, S. X. Yu, J. Shi, Multiclass Spectral Clustering, in: *In International Conference on*
463 *Computer Vision*, 2003, pp. 313–319.
- 464 [31] T. E. J. Behrens, H. Johansen-Berg, M. W. Woolrich, S. M. Smith, C. a. M. Wheeler-Kingshott,
465 P. A. Boulby, G. J. Barker, E. L. Sillery, K. Sheehan, O. Ciccarelli, A. J. Thompson, J. M. Brady,
466 P. M. Matthews, Non-invasive mapping of connections between human thalamus and cortex using
467 diffusion imaging, *Nature Neuroscience* 6 (7) (2003) 750–757. doi:10.1038/nn1075.
- 468 [32] D. M. Cash, M. Bocchetta, D. L. Thomas, K. M. Dick, J. C. van Swieten, B. Borroni, D. Galimberti,
469 M. Masellis, M. C. Tartaglia, J. B. Rowe, C. Graff, F. Tagliavini, G. B. Frisoni, J. Laforce, Robert,
470 E. Finger, A. de Mendonça, S. Sorbi, M. N. Rossor, S. Ourselin, J. D. Rohrer, Patterns of gray
471 matter atrophy in genetic frontotemporal dementia: results from the GENFI study, *Neurobiology*
472 *of Aging* 62 (2018) 191 – 196.

473 List of other GENFI consortium members

474 Christin Andersson - Department of Clinical Neuroscience, Karolinska Institutet,
475 Stockholm, Sweden

476 Silvana Archetti - Biotechnology Laboratory, Department of Diagnostics, Civic Hos-
477 pital of Brescia, Brescia, Italy
478 Andrea Arighi - Neurology Unit, Department of Physiopathology and Transplanta-
479 tion, Fondazione C Granda, Istituto di Ricovero e Cura a Carattere Scientifico Ospedale
480 Policlinico, Milan, Italy
481 Luisa Benussi - Istituto di Ricovero e Cura a Carattere Scientifico Istituto Centro
482 San Giovanni di Dio Fatebenefratelli, Brescia, Italy
483 Sandra Black - LC Campbell Cognitive Neurology Research Unit, Sunnybrook Re-
484 search Institute, Toronto, Canada
485 Maura Cosseddu - Centre of Brain Aging, University of Brescia, Brescia, Italy
486 Marie Fallstrm - Department of Geriatric Medicine, Karolinska University Hospital,
487 Stockholm, Sweden
488 Carlos Ferreira - Instituto Cincias Nucleares Aplicadas Sade, Universidade de Coim-
489 bra,Coimbra, Portugal
490 Chiara Fenoglio - Dept. of Pathophysiology and Transplantation, "Dino Ferrari" Cen-
491 ter, University of Milan, Fondazione C Granda, IRCCS Ospedale Maggiore Policlinico,
492 Milan, Italy
493 Nick Fox - Dementia Research Centre, UCL Institute of Neurology, London, UK
494 Morris Freedman - Division of Neurology, Baycrest Centre for Geriatric Care, Uni-
495 versity of Toronto, Canada
496 Giorgio Fumagalli - Neurology Unit, Fondazione C Granda, Istituto di Ricovero e
497 Cura a Carattere Scientifico Ospedale Policlinico, Milan, Italy
498 Stefano Gazzina - Centre of Brain Aging, Neurology Unit, Department of Clinical
499 and Experimental Sciences, University of Brescia, Brescia, Italy
500 Roberta Ghidoni - Istituto di Ricovero e Cura a Carattere Scientifico Istituto Centro
501 San Giovanni di Dio Fatebenefratelli, Brescia, Italy
502 Marina Grisoli - Fondazione Istituto di Ricovero e Cura a Carattere Scientifico Istituto
503 Neurologico Carlo Besta, Milano, Italy
504 Vesna Jelic - Division of Clinical Geriatrics, Karolinska Institutet, Stockholm, Sweden
505 Lize Jiskoot - Department of Neurology, Erasmus Medical Center, Rotterdam, The
506 Netherland
507 Ron Keren - University Health Network Memory Clinic, Toronto Western Hospital,
508 Toronto, Canada
509 Gemma Lombardi - Department of Neuroscience, Psychology, Drug Research and
510 Child Health, University of Florence, Florence, Italy
511 Carolina Maruta - Lisbon Faculty of Medicine, Language Research Laboratory, Lis-
512 bon, Portugal
513 Lieke Meeter - Department of Neurology, Erasmus Medical Center, Rotterdam, The
514 Netherlands
515 Rick van Minkelen - Department of Clinical Genetics, Erasmus Medical Center, Rot-
516 terdam, The Netherland
517 Benedetta Nacmias - Department of Neuroscience, Psychology, Drug Research and
518 Child Health, University of Florence, Florence, Italy
519 Linn ijerstedt - Division of Neurogeriatrics, Karolinska Institutet, Stockholm, Sweden
520 Alessandro Padovani - Neurology Unit, Department of Medical and Experimental
521 Sciences, University of Brescia, Brescia, Italy

522 Jessica Panman - Department of Neurology, Erasmus Medical Center, Rotterdam,
523 The Netherland
524 Michela Pievani - Istituto di Ricovero e Cura a Carattere Scientifico Istituto Centro
525 San Giovanni di Dio Fatebenefratelli, Brescia, Italy
526 Cristina Polito - Department of Clinical Pathophysiology, University of Florence,
527 Florence, Italy
528 Enrico Premi - Centre for Ageing Brain and Neurodegenerative Disorders, Neurology
529 Unit, University of Brescia, Brescia, Italy
530 Sara Prioni - Fondazione Istituto di Ricovero e Cura a Carattere Scientifico Istituto
531 Neurologico Carlo Besta, Milano, Italy
532 Rosa Rademakers - Department of Neurosciences, Mayo Clinic, Jacksonville, Florida
533 Veronica Redaelli - Fondazione Istituto di Ricovero e Cura a Carattere Scientifico
534 Istituto Neurologico Carlo Besta, Milano, Italy
535 Ekaterina Rogueva - Tanz Centre for Research in Neurodegenerative Diseases, Uni-
536 versity of Toronto, Canada
537 Giacomina Rossi - Fondazione Istituto di Ricovero e Cura a Carattere Scientifico
538 Istituto Neurologico Carlo Besta, Milano, Italy
539 Martin Rossor - Dementia Research Centre, UCL Institute of Neurology, London, UK
540 Elio Scarpini - Neurology Unit, Department of Physiopathology and Transplanta-
541 tion, Fondazione C Granda, Istituto di Ricovero e Cura a Carattere Scientifico Ospedale
542 Policlinico, Milan, Italy
543 David Tang-Wai - University Health Network Memory Clinic, Toronto Western Hos-
544 pital, Toronto, Canada
545 Carmela Tartaglia - Tanz Centre for Research in Neurodegenerative Diseases, Uni-
546 versity of Toronto, Canada
547 Hakan Thonberg - Center for Alzheimer Research, Division of Neurogeriatrics, Karolin-
548 ska Institutet, Stockholm, Sweden
549 Pietro Tiraboschi - Fondazione Istituto di Ricovero e Cura a Carattere Scientifico
550 Istituto Neurologico Carlo Besta, Milano, Italy
551 Ana Verdelho - Department of Neurosciences, Santa Maria Hospital, University of
552 Lisbon, Portugal
553 Jason Warren - Dementia Research Centre, UCL Institute of Neurology, London, UK